AGU PUBLICATIONS

Geochemistry, Geophysics, Geosystems

RESEARCH ARTICLE
10.1002/2014GC005569

Influence of late Pleistocene glaciations on the hydrogeology of the continental shelf offshore Massachusetts, USA

Jacob Siegel[1], Mark Person[2], Brandon Dugan[1], Denis Cohen[3], Daniel Lizarralde[4], and Carl Gable[5]

[1]Department of Earth Science, Rice University, Houston, Texas, USA, [2]Department of Earth and Environmental Sciences, New Mexico Institute of Mining and Technology, Socorro, New Mexico, USA, [3]Department of Geology and Atmospheric Sciences, Iowa State University, Ames, Iowa, USA, [4]Department of Geology and Geophysics, Woods Hole Oceanographic Institution, Woods Hole, Massachusetts, USA, [5]Los Alamos National Laboratory, Los Alamos, New Mexico, USA

Key Points:
- 3-D numerical modeling of continental shelf offshore Massachusetts, USA
- Incorporate 3-D stratigraphy, glaciations, and sea level history into modeling
- Modeling results show freshwater extends 30 km beyond Martha's Vineyard, MA

Correspondence to:
B. Dugan,
dugan@rice.edu

Citation:
Siegel, J., M. Person, B. Dugan, D. Cohen, D. Lizarralde, and C. Gable (2014), Influence of late Pleistocene glaciations on the hydrogeology of the continental shelf offshore Massachusetts, USA, *Geochem. Geophys. Geosyst.*, *15*, 4651–4670, doi:10.1002/2014GC005569.

Received 4 SEP 2014
Accepted 12 OCT 2014
Accepted article online 30 OCT 2014
Published online 5 DEC 2014

Abstract Multiple late Pleistocene glaciations that extended onto the continental shelf offshore Massachusetts, USA, may have emplaced as much as 100 km^3 of freshwater (salinity $<$5 ppt) in continental shelf sediments. To estimate the volume and extent of offshore freshwater, we developed a three-dimensional, variable-density model that couples fluid flow and heat and solute transport for the continental shelf offshore Massachusetts. The stratigraphy for our model is based on high-resolution, multichannel seismic data. The model incorporates the last 3 Ma of climate history by prescribing boundary conditions of sea level change and ice sheet extent and thickness. We incorporate new estimates of the maximum extent of a late Pleistocene ice sheet to near the shelf-slope break. Model results indicate that this late Pleistocene ice sheet was responsible for much of the emplaced freshwater. We predict that the current freshwater distribution may reach depths up to 500 meters below sea level and up to 30 km beyond Martha's Vineyard. The freshwater distribution is strongly dependent on the three-dimensional stratigraphy and ice sheet history. Our predictions improve our understanding of the distribution of offshore freshwater, a potential nonrenewable resource for coastal communities along recently glaciated margins.

1. Introduction

Freshwater resources are important for agriculture, industry, and domestic use; however, many freshwater resources, particularly groundwater, are declining [*Barlow*, 2003]. In coastal regions, freshwater resources are vulnerable to change as climate and sea level change [*Ferguson and Gleeson*, 2012] because sea level influences the position of the freshwater-salt water interface [*Post et al*., 2013]. Investigations of freshwater in deep sedimentary basins throughout northern North America show that much of the subsurface freshwater was emplaced during Pleistocene glaciations and is not in equilibrium with current meteoric recharge [*Person et al*., 2007a; *Lemieux et al*., 2008a; *McIntosh et al*., 2012; *Neuzil*, 2012; *Person et al*., 2012; *Post et al*., 2013]. These basins were all beneath or near the edge of the Laurentide ice sheet, and enhanced freshwater emplacement associated with ice sheets may explain the origin of the deep freshwater [*McIntosh and Walter*, 2005; *Bense and Person*, 2008; *McIntosh et al*., 2011].

Evidence of glacially emplaced freshwater into the basins comes from many sources [*Post et al*., 2013]. Age data from carbon-14 and noble gases reveal a Pleistocene age for much of the freshwater [*Morrissey et al*., 2010; *Schlegel et al*., 2011], and oxygen isotope data reveal isotopically light freshwater which is interpreted as water of glacial origin [*Vaikmae et al*., 2001; *McIntosh et al*., 2012]. In addition, numerical models indicate large volumes of subglacial meltwater may have been driven into basin sediments during Pleistocene glaciations [*Person et al*., 2007a, 2012; *Post et al*., 2013].

Sedimentary basins on the northern U.S. Atlantic continental shelf experienced glaciations in the late Pleistocene in combination with sea level change throughout the Pleistocene [*Oldale and O'Hara*, 1984; *Uchupi et al*., 2001; *Siegel et al*., 2012]. Sea level change is another mechanism that can drive freshwater emplacement [*Meisler et al*., 1984; *Kooi et al*., 2000]. A combination of climate-driven sea level change and glaciations has been implicated as the source of freshwater as far as 100 km offshore New Jersey that reaches depths of several hundred meters below the seafloor (mbsf) [*Hathaway et al*., 1979; *Kohout et al*., 1988; *Cohen et al*., 2010; *Post et al*., 2013]. On Nantucket Island, offshore Massachusetts, freshwater extends to depths greater

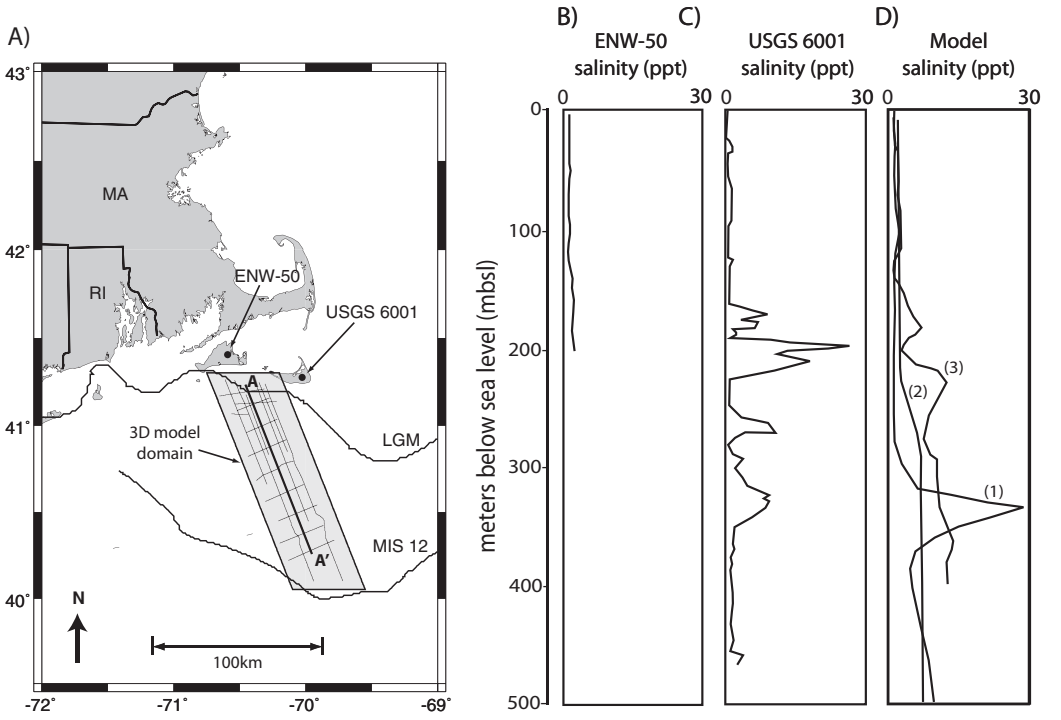

Figure 1. (a) Regional basemap showing seismic lines used in this study and plan view of the three-dimensional model space (light gray box). Maximum extents of the Last Glacial Maximum (LGM) and Marine Oxygen Isotope Stage (MIS) 12 ice sheets (thick black lines) and USGS 6001 and ENW-50 wells (black dots) are shown for reference. Pore water salinity determined at wells (b) ENW-50 and (c) USGS 6001. (d) Model-predicted salinity for well USGS 6001 determined by previous numerical models that assumed sea level change and Pleistocene ice sheets boundary conditions: (1) *Person et al.* [2003], (2) *Cohen et al.*, [2010], and (3) *Marksamer et al.* [2007].

than 500 meters below sea level (mbsl; Figure 1) [*Kohout et al.*, 1977; *Folger et al.*, 1978]. The extent of this freshwater offshore Massachusetts is unknown.

Several two-dimensional and three-dimensional numerical modeling studies have predicted freshwater distributions for the continental shelf offshore New England. These models incorporated sea level change and ice sheets as boundary conditions in an effort to explain salinity patterns observed below Nantucket Island, and to predict the volume and distribution of offshore freshwater (Figure 1d) [*Person et al.*, 2003; *Marksamer et al.*, 2007; *Cohen et al.*, 2010]. These studies were based on limited well data and low-resolution seismic reflection data, which do not allow for detailed stratigraphic or bathymetric features to be resolved and used as model inputs. Recent high-resolution, multichannel seismic reflection data offshore Massachusetts provide high quality bathymetry and new insights into the continental shelf stratigraphy and the seaward extent of glaciations. We use these new stratigraphic, bathymetric, and glacial interpretations as inputs to a three-dimensional, finite element, variable-density numerical model that couples fluid flow and heat and solute transport to better estimate freshwater volume beneath the Massachusetts continental shelf. This is the first time it is possible to represent the true three-dimensional stratigraphy offshore Massachusetts based on direct seismic observations. Therefore, we have enhanced capability to understand the impacts of three-dimensional stratigraphy, sea level cycles, and transient ice sheet loading on the distribution and the volumes of offshore freshwater.

We explore four model scenarios to understand basic hydrogeologic behavior and the emplaced volumes of freshwater: a base-case scenario and three different permeability scenarios. The base case is derived from our seismic-stratigraphic interpretations. The three permeability variations are (1) a system with a lower permeability for the near-surface glacial sediments; (2) a system with a higher-permeability deep carbonate unit; and (3) a simplified lithologic model that only employs two permeability values. Each scenario is then studied for time-varying sea level histories and three separate glacial histories (no glaciers, only the Last Glacial Maximum [LGM] glacial advance, and five glacial advances in the last 500 ka). With our simulations of coupled fluid flow and heat and solute transport, we show that the previously unrecognized extent

of a late Pleistocene ice sheet advance resulted in as much as 100 km^3 of emplaced freshwater as far as 30 km offshore. The distribution of the freshwater, however, is strongly dependent on the three-dimensional stratigraphy and ice loading history.

2. Geologic Background

2.1. Pleistocene Climate

North American glaciations began at the end of the Pliocene, about 2.7 Ma B.P. [*Bintanja and van de Wal*, 2008; *Balco and Rovey*, 2010]. In the late Pliocene and early Pleistocene, 2.7–1.25 Ma B.P., sea level change had an average amplitude $<$80 m and a period of 41 ka [*Ruddiman et al*., 1986; *Williams et al*., 1988; *Huybers*, 2007]. In the middle Pleistocene, 1.25–0.7 Ma B.P., sea level change gradually increased in amplitude to 120 m and had dominant periods of 41 and 100 ka [*Huybers*, 2007]. In the late Pleistocene, 0.7–0.012 Ma B.P., sea level change had an average amplitude of 120 m and a dominant period of 100 ka. In the late Pleistocene, North American ice sheets had their greatest thickness and largest extent [*Piper et al*., 1994; *Bintanja and van de Wal*, 2008].

2.2. Stratigraphy, Glacial History, and Pore Water Geochemistry

Siegel et al. [2012] identified seven stratigraphic units offshore Massachusetts that span the Cretaceous to the Holocene (Figure 2). The units show significant variability in stratigraphic thickness downdip and along strike. Unit 1 formed from slow, pelagic sedimentation during the Cretaceous and likely consists of carbonate sands. Unit 2 formed from slow, pelagic sedimentation during the Paleocene and Eocene and likely consists of carbonate mud and sand. Unit 3 formed from increased siliciclastic input during the Oligocene and Miocene [*Steckler et al*., 1999] and likely consists of silt and clay clinoforms. Unit 4 formed from rapidly deposited glacigenic sediments during the late Pleistocene and likely consists of poorly sorted silts and clays. Units 5 and 6 formed from high siliciclastic input with deposition responding to high-amplitude sea level change during the late Pleistocene [*Metzger et al*., 2000] and likely consist of sand, silt, and clay clinoforms. Unit 7 formed from siliciclastic sedimentation and glacial outwash during the late Pleistocene and Holocene and likely consists of sand and silt.

Two regional unconformities (U1 and U2) are also present in the study region. U1 (Figure 2b) is interpreted as a marine oxygen isotope stage (MIS) 12 glacial unconformity and marks the first Pleistocene shelf-crossing glaciation offshore Massachusetts [*Siegel et al*., 2012]. Several additional glacial advances occurred throughout the late Pleistocene, although their extent onto the shelf was less, probably terminating near the maximum extent of the Laurentide ice sheet during the LGM (Figure 1) [*Oldale and O'Hara*, 1984; *Uchupi et al*., 2001]. U2 is a shallow sequence boundary that formed during the last sea level fall (40–30 ka B.P.).

Pore water geochemical analysis from Atlantic Margin Coring Project (AMCOR) and U.S. Geological Survey (USGS) wells offshore New England and New Jersey and on Martha's Vineyard and Nantucket Island (Figure 1) document freshwater that extends nearly 100 km offshore (AMCOR Site 6009 offshore New Jersey) and reaches depths up to 500 mbsl (Well USGS 6001 on Nantucket Island) [*Kohout et al*., 1977; *Folger et al*., 1978; *Hathaway et al*., 1979; *Kohout et al*., 1988]. Well USGS 6001 on Nantucket Island shows several stratigraphic zones with varying salinity: from 7.3 to 150 mbsl, salinity is generally $<$1 part per thousand (ppt) in a predominantly sand and gravel layer; from 150 to 360 mbsl, there is an irregular pattern of salinity ranging from 1 to 29 ppt (seawater is 35 ppt), where freshwater is predominantly in sands and salt water is in clays; below 360 mbsl, there is a zone of freshwater (salinity of 2–3 ppt) in a large sand body. The freshwater in well USGS 6001 is much deeper than that predicted by the Ghyben-Herzberg principle [*Kohout et al*., 1977; *Marksamer et al*., 2007]. *Person et al*. [2003] hypothesize that glaciations on the Massachusetts shelf flushed salt water from permeable units near shore, resulting in the salinity pattern observed in the USGS 6001 well and in the ENW-50 well on Martha's Vineyard (Figure 1).

3. Previous Continental Shelf Hydrogeologic Modeling Studies

Several modeling studies of the continental shelf offshore Massachusetts simulated fluid flow and solute transport with Pleistocene boundary conditions (e.g., sea level change, ice sheets, permafrost, and proglacial lakes) to estimate the offshore distribution of freshwater and to explain the salinity observed in well USGS 6001 [*Person et al*., 2003; *Marksamer et al*., 2007; *Cohen et al*., 2010; *DeFoor*, 2011]. These models used

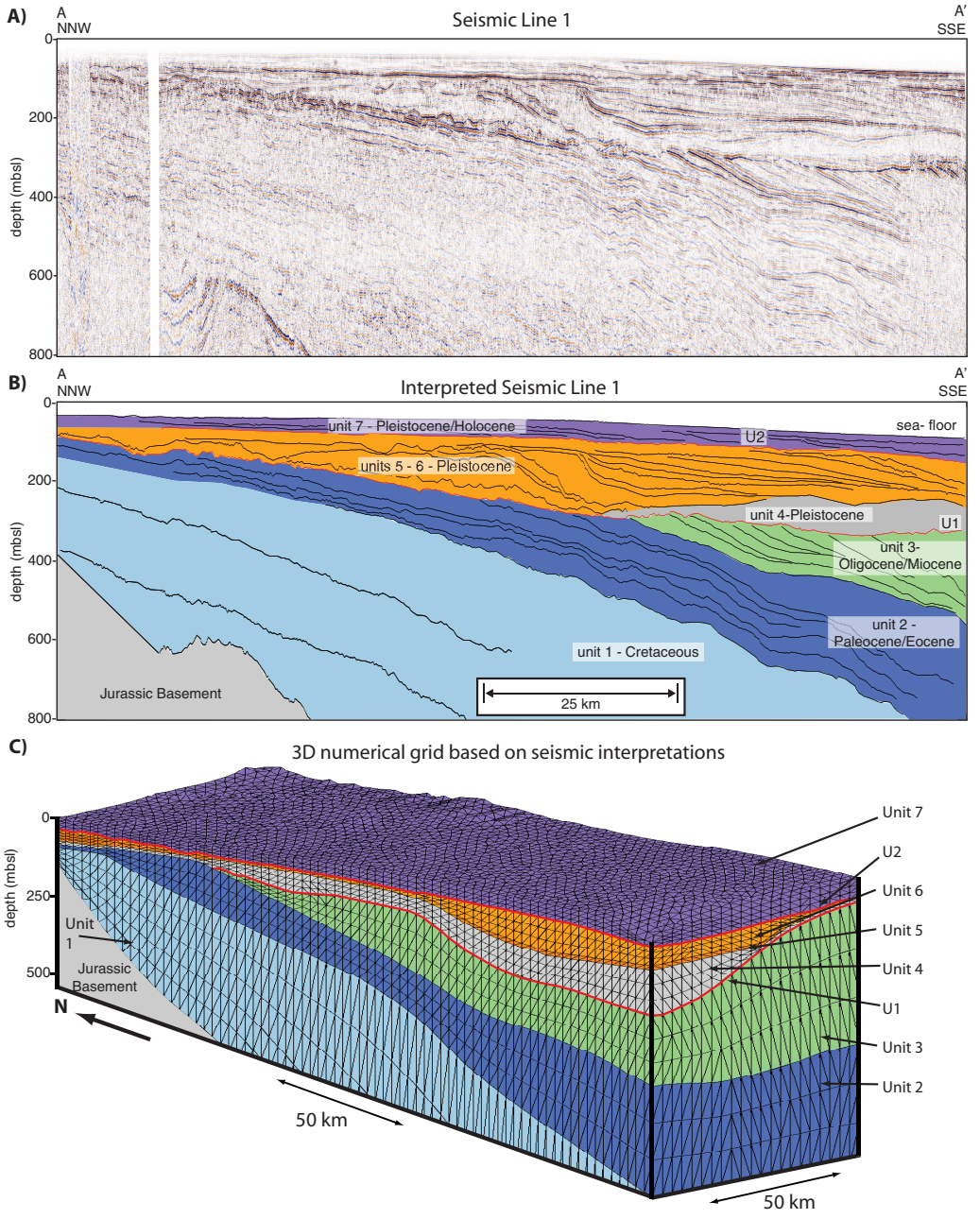

Figure 2. (a) Uninterpreted seismic line A–A′, located in Figure 1. (b) Interpreted seismic line A–A′ showing interpreted age and lithologic units. (c) Numerical grid used in three-dimensional modeling; colors correspond to lithologic units in Figure 2b. The depth of the grid extends to 3500 m in the south.

different assumptions of ice sheet extent and timing, sea level change, and stratigraphy, which resulted in different salinity patterns (Figure 1d). One consistency, however, was that all the studies showed large volumes of freshwater were emplaced offshore due to the combined effects of Pleistocene sea level change and glaciations.

Person et al. [2003] modeled a two-dimensional transect from onshore Massachusetts through Nantucket Island to the shelf-slope break. They employed a simplified lithology with alternating layers of sand and silt/clay, and they assumed permafrost extended 50 km beyond the ice sheet edge. Sea level was prescribed as a sinusoid with a 100 ka period and a 120 m amplitude. Their models predicted that freshwater recharge during sea level lowstands was not enough to emplace the deep freshwater observed at well USGS 6001.

Table 1. Lithologic Units, Interpreted Age and Lithology, Permeability (k), and Porosity (ϕ) for the Base-Case (BC) Models[a]

Unit	Age and Lithology	k_x (m^2)	ϕ
7	Late Pleistocene/Holocene: glacial outwash	10^{-13}	0.3
6	Late Pleistocene: sand, silt, clay clinoforms	10^{-15}	0.2
5	Late Pleistocene: thin clay layer	10^{-17}	0.2
4	Late Pleistocene: glacigenic sediments	10^{-15}	0.3
3	Oligocene/Miocene: silt/clay clinoforms	$10^{-17}/10^{-14}/10^{-17}$[b]	0.2
2	Paleocene/Eocene: carbonate mud	10^{-15}	0.2
1	Cretaceous: carbonate sandstone	10^{-14}	0.3

[a]Anisotropy: vertical/horizontal permeability (k_z/k_x) = 0.1.
[b]Unit 3 contains three clinoforms.

When they imposed ice cover and associated subglacial recharge for 1 ka during the LGM, freshwater flushed aquifers and their models matched the salinity pattern at well USGS 6001 at 375 mbsl; however, due to the simplified stratigraphy, the model did not match the entire salinity profile at well USGS 6001 (Figure 1d).

Marksamer et al. [2007] modeled a similar two-dimensional transect to that of *Person et al*. [2003], but their stratigraphy included more detail, containing five stratigraphic units based on the lithology at well USGS 6001. They incorporated sediment loading, permafrost, and proglacial lakes, and modeled the Laurentide ice sheet during the LGM. Sea level was prescribed as a sinusoid with a 100 ka period and a 120 m amplitude. Their results also indicate that differential loading and lateral flow driven by ice sheet loading was necessary to drive freshwater offshore. The refined stratigraphy improved the match of salinity variation between stratigraphic layers when comparing observed and modeled salinity; however, modeled salinity increased with depth, which is not observed in well USGS 6001 (Figure 1d).

Cohen et al. [2010] constructed a three-dimensional model to represent the continental shelf from offshore New Jersey to offshore Maine to assess the regional distribution of freshwater in the continental shelf. The large model extent prevented the use of detailed stratigraphy, so they only included three lithologic units (medium-coarse sands, fine sands, and silt/clays). They, however, included three Pleistocene glacial cycles (Wisconsin, Nebraskan, and Illinoian) and assumed each had a regional glacial extent identical to the LGM. Sea level was based on an isotopically derived sea level curve [*Imbrie et al*., 1984] for the past 200 ka and repeated for the entire Pleistocene with a 120 m amplitude. Thus, they incorporated short-period (several thousand year) sea level changes as observed in the isotopic record; however, they did not capture the general trend of Pleistocene sea level change period transitioning from 41 to 100 ka. Their results showed that in glaciated regions (i.e., offshore Massachusetts and Maine), freshwater emplacement was primarily in sand, however, there were no localized zones of salt water predicted at well USGS 6001 (Figure 1d).

4. Numerical Modeling for This Study

We use a three-dimensional, finite element, numerical model to simulate variable-density groundwater flow and heat and solute transport for the Massachusetts continental shelf from the end of the Pliocene through the Holocene (3 Ma). Our model includes five late Pleistocene glaciations that extended onto the shelf. This model allows us to explore the complex influences of climate cycles and three-dimensional stratigraphy on offshore freshwater emplacement and distribution. Modeling heat flow allows us to explore the potential for convection-induced fluid and solute mixing due to geothermal heat transport from depth and recharge by cool subglacial water from the surface. We use PGEOFE, a parallel version of GEOFE, which is a serial, finite element-based paleohydrogeologic model [*Person et al*., 2007b; *Cohen et al*., 2010].

4.1. Model Domain

Our numerical grid is based on the seismic and lithologic interpretations of *Siegel et al*. [2012] (Figure 2). The base of the model is defined by the depth to the top of Jurassic basement (Figure 2), which is interpreted as basalt based on its high P wave velocity [*Siegel et al*., 2012] and sampled Jurassic basalt at 460 mbsl on Nantucket Island well USGS 6001 [*Folger et al*., 1978]. Without constraints on the structure or thickness of the Jurassic basalt and to focus on the sedimentary section, we treat the basalt as a no flow boundary. Seven lithologic units overlie the Jurassic basement (Figure 2). The physical properties of these units are based on interpreted sediment type (Table 1) and are referred to as the base-case (BC) model. The

Table 2. Parameters Used in All Simulations

Model Parameters	Symbol	Value	References
Heat capacity of fluid	c_f	4128 J kg^{-1} K^{-1}	*Bense and Person* [2008]
Heat capacity of solid	c_s	1870 J kg^{-1} K^{-1}	*Bense and Person* [2008]
Longitudinal dispersivity	α_L	100 m	*Cohen et al.* [2010]
Transversal dispersivity	α_T	10 m	*Cohen et al.* [2010]
Density of solid grain	ρ_s	2650 kg m^{-3}	*Lambe and Whitman* [1969]
Density of water at standard state	ρ_o	1000 kg m^{-3}	*Marksamer et al.* [2007]
Density of ice	ρ_i	900 kg m^{-3}	*Bense and Person* [2008]
Solute diffusivity	D_m	10^{-9} m^2 s^{-1}	*Freeze and Cherry* [1979]
Solid thermal conductivity	κ_s	2.5 W m^{-1} K^{-1}	*Spinelli et al.* [2007]
Fluid thermal conductivity	κ_f	0.58 W m^{-1} K^{-1}	*Bense and Person* [2008]
Specific storage	S_s	10^{-3} m^{-1}	*Cohen et al.* [2010]; *Siegel et al.* [2014]

permeability and physical properties we select are based on previous modeling studies [*Marksamer et al.*, 2007; *Person et al.*, 2003; *Cohen et al.*, 2010; *Siegel et al.*, 2014] to allow comparison with previous studies. In addition, we varied permeability to explore the impacts of permeability architecture and uncertainty on the extent, distribution, and volume of offshore freshwater (see section 5.3).

We used a grid that contains 32,021 nodes and 172,167 tetrahedral elements that were generated by LaGrit [*Gable et al.*, 1996]. The horizontal node spacing averages 2 km while the vertical node spacing ranges from 10 m in the near surface to 400 m in the deeper subsurface. We use the more refined vertical discretization in the near surface to insure there is enough grid resolution in the thin upper model units to avoid numerical dispersion.

4.2. Fluid Flow

We solve the following groundwater flow equation, which describes variable-density fluid flow and incorporates the effects of ice sheet loading [*Cohen et al.*, 2010; *Person et al.*, 2012]:

$$\nabla \cdot \left[\frac{k\rho_o g}{\mu_f}\mu_r \nabla(h+\rho_r z)\right] = S_s\left[\frac{\partial h}{\partial t} - \frac{\rho_i}{\rho_o}\frac{\partial \eta}{\partial t}\right], \quad (1)$$

where ∇ is the gradient operator, k is intrinsic permeability, ρ_o is density of water at the standard state (10°C, salinity of 0 ppt, and atmospheric pressure), g is acceleration due to gravity, μ_f is viscosity of water at elevated temperature, pressure, and salinity conditions, μ_r is relative viscosity ($\mu_r = \mu_o/\mu_f$), μ_o is viscosity of water at the standard state, h is hydraulic head relative to a reference datum of modern sea level (0.0 m), ρ_r is relative density ($\rho_r = (\rho_f - \rho_o)/\rho_o$), ρ_f is density of water at elevated temperature, pressure, and salinity conditions, z is elevation relative to a reference datum of modern sea level (0.0 m), S_s is specific storage, t is time, ρ_i is ice density, and η is ice sheet thickness (see Tables 1 and 2 for model parameters). Equation (1) is similar to a standard equation for variable-density groundwater flow [e.g., *Ingebritsen et al.*, 2007], modified to account for the effects of ice sheet loading ($\partial\eta/\partial t$). When the ice sheet is present, we assume a loading efficiency of 1, which means the stress from the ice sheet results in an increase in subsurface pore pressure equal to the applied stress from the ice sheet [*Lemieux et al.*, 2008b]. We do not account for the effects of sedimentation, which was shown to have little effect on salinity distribution [*DeFoor*, 2011]. The sides and base of the model are no flow boundaries. Treating the landward and seaward boundaries as no flow boundaries provides an end-member case that is conservative with respective to fluid flow and solute transport. The landward no flow boundary prevents meteoric or subglacial waters from entering through the landward model boundary. As topography increases landward and the glacial load thickens landward, this boundary condition provides a minimum input of freshwater into the model domain. The no flow seaward boundary is also conservative for freshwater fluxes. Allowing fluxes across the domain with direct pathways to the ocean enhances lateral transport and increases the offshore extent of the freshwater distribution [*Cohen et al.*, 2010]. During simulations, the head for the top boundary is equal to sea level for subsea surface nodes, equal to land surface elevation for subaerial surface nodes, and controlled by glacial thickness for surface nodes beneath the modeled glacier (see sections 4.5 and 4.6). The initial condition is hydrostatic fluid pressure for the entire model domain.

Fluid density (ρ_f) and viscosity (μ_f) are functions of pressure, solute concentration, and temperature. This relationship is defined by thermodynamic equations of state determined by *Kestin et al.* [1981].

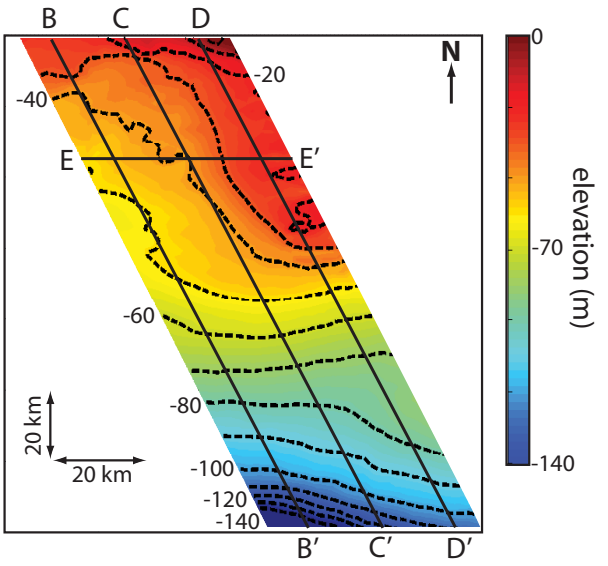

Figure 3. Surface elevation of our three-dimensional grid and the location of the cross sections shown in Figures 6, 7, and 10–12. The upper right-hand corner (northeast corner), which represents Nantucket Island, is 1–3 meters above sea level. The dashed lines are elevation contours in 10 m intervals. Locations of the 3-D model domain and seismic lines are shown in Figure 1. Model cross section C–C′ is equivalent to seismic cross section A–A′ (Figures 1 and 2).

4.3. Solute Transport

Solute transport is determined from the advection-diffusion equation [e.g., *Ingebritsen et al.*, 2007; *Cohen et al.*, 2010]:

$$\phi \frac{\partial C}{\partial t} = \nabla(\phi D \nabla C) - \vec{q} \nabla C, \quad (2)$$

where ϕ is porosity, C is solute concentration, D is a three-dimensional hydrodynamic dispersion-diffusion tensor for porous medium which is a function of longitudinal and transverse dispersivity and solute diffusivity (see Table 2 for model parameters) [*Konikow and Grove*, 1977], and $\vec{q}$ is the specific discharge vector.

$$\vec{q} = -\frac{k\rho_o g}{\mu_f} \mu_r \nabla(h + \rho_r z). \quad (3)$$

We model the total dissolved solid concentration and report it as mass fraction (parts per thousand).

The initial pore water salinity is 35 ppt throughout the model. During the model simulation, subaerial surface nodes with downward fluid flow are assigned freshwater salinity (0 ppt), and subsea surface nodes with downward fluid flow are assigned seawater salinity (35 ppt). The sides and base of the model have no salinity exchange.

4.4. Heat Transport

Heat transport is determined from the conductive and convective-dispersive heat transfer equation [*Cohen et al.*, 2010]:

$$[c_f \rho_f \phi + c_s \rho_s (1-\phi)] \frac{\partial T}{\partial t} = \nabla[\lambda \nabla T] - \vec{q} \rho_f c_f \nabla T, \quad (4)$$

where c_s and c_f are the specific heat capacities of the solid and liquid phases, respectively, ρ_s is the density of the solid phase, T is temperature, and λ is the thermal dispersion-conduction tensor, which is a function of solid and fluid thermal conductivity, porosity, longitudinal and transverse dispersivities, fluid density, fluid heat capacity, and the specific discharge vector (see Table 2 for model parameters) [*de Marsily*, 1986].

The initial temperature is 4°C at the surface with a gradient of 30°C km^{-1}. During the simulation, subaerial surface nodes have a constant temperature of 5°C, and subaqueous surface nodes have a constant temperature of 4°C. The base of the model has a constant heat flux of 0.06 W m^{-2}. The sides of the model have thermally insulated boundary conditions.

4.5. Sea Level Boundary Condition

The sea level boundary condition is applied by assigning surface nodes above sea level a hydraulic head equal to the surface elevation (Figure 3) while surface nodes below sea level are assigned a hydraulic head equal to sea level. We start the simulation with a sinusoidal sea level curve for 1 Ma (Figure 4a). Then, we prescribe an idealized, 2 Ma Pleistocene sea level curve (Figure 4b). For the Pleistocene sea level curve, we assume sea level fall is 80% of a cycle in the early and middle Pleistocene and 85% of a cycle in the late Pleistocene [*Lisiecki and Raymo*, 2007]. Periodicity is 41 ka in the early Pleistocene, 100 ka in the late Pleistocene, and a combination of the two in the middle Pleistocene. Maximum sea level fall (relative to modern) is 85 m in the early Pleistocene, 120 m in the late Pleistocene, and varying with a range between 85 and 120 m the in the middle Pleistocene.

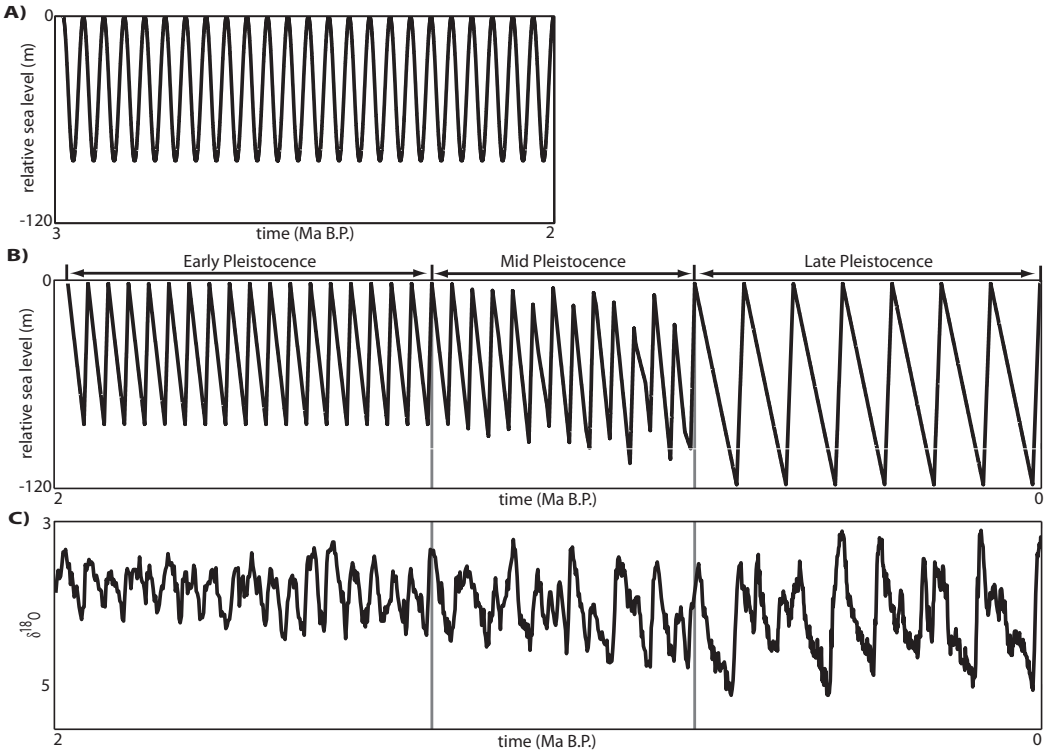

Figure 4. (a) Sinusoidal sea level curved used to initialize models. (b) Idealized 2 Ma Pleistocene sea level curved used in all models. (c) Stacked marine oxygen isotope data [*Lisiecki and Raymo*, 2005], which is a proxy for the general trends in sea level period and amplitude in the Pleistocene.

4.6. Ice Sheet Boundary Condition

We prescribe the ice sheet boundary as a time series of ice sheet thickness and extent that represents the late Pleistocene glacial history on the shelf based on geophysical interpretations of an MIS 12 ice sheet that reached the shelf edge [*Siegel et al.*, 2012] and the LGM ice sheet [*Uchupi et al.*, 2001]. We assume that the MIS 12 glaciation was followed by four glacial advances identical in extent to the LGM (Figure 5a). Hydraulic head at the base of the ice sheet is 90% that of the ice sheet height [*Boulton and Caban*, 1995]. This assumes a wet-based ice sheet, which is consistent with the interpretation that this region had an active ice sheet-ice stream system [*Siegel et al.*, 2012]. The height profile of the ice sheet is a polynomial expression [*van der Veen*, 1998]:

$$\eta = H\sqrt{1-(\xi/L)^2}, \tag{5}$$

where η is the height of the ice sheet at a particular location (node) which is a distance (ξ) from the center of the ice sheet. H and L are the maximum ice sheet thickness and length at a particular time step and reflect the change in size of the ice sheet over a glacial cycle. The maximum thickness prescribed for the MIS 12 ice sheet is 1200 m (Figure 5b) based on the minimum ice sheet thickness (275 m) interpreted at the shelf edge [*Siegel et al.*, 2012]. The maximum thickness prescribed for the remaining ice sheets is 500 m (Figure 5b) based on numerical models of the LGM [*Marshall et al.*, 2002]. The ice sheets build from the northern edge of the model and advance to the south. The late Pleistocene ice sheets were only on the shelf for several tens of thousands of years, a timeframe comparable to the timescale for isostatic adjustment [e.g., *Peltier and Andrews*, 1976; *Peltier*, 2011]. In our simulations, model nodes are deflected downward by 20% of the ice sheet thickness [*Cohen et al.*, 2010].

5. Results

5.1. Sea Level Change

Our initial simulation with the base-case model parameters (Table 1) considers the impacts of Pleistocene sea level change (Figure 4) as a freshwater-forcing mechanism on the shelf in the absence of glaciations

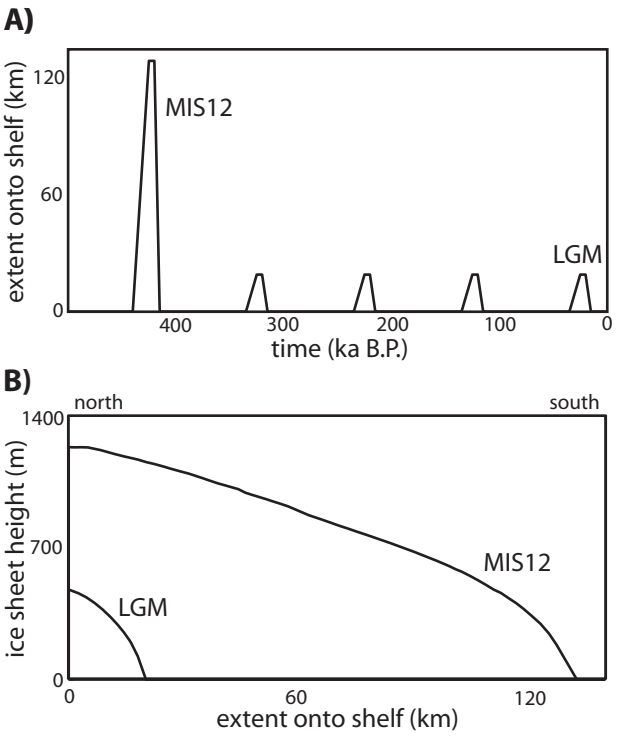

Figure 5. (a) Ice sheet time series showing the assumed extent of the late Pleistocene ice sheets onto the continental shelf past the northern edge of the model domain. (b) Cross-sectional profile of maximum ice sheet height and extent onto the shelf for the Last Glacial Maximum (LGM) and Marine Oxygen Isotope Stage (MIS) 12 ice sheets.

(Figure 6a). Sea level change results in 18 km^3 of predicted, present-day freshwater (salinity <5 ppt) in the shelf system (1.1% of total fluid volume in our model domain). This estimate assumes freshwater-saturated sediments have a porosity of 0.2–0.3 (Table 1). The northern edge of the model domain has salinity <5 ppt (Figure 6a), and the average salinity of the model domain is 24.2 ppt (Table 3). Salinity also correlates with the surface elevation, with the eastern side of the model (20 m higher elevation) being fresher than the western side (Figure 7a).

The average salinity of the system decreased with time after each sea level cycle (Figure 8). The time of highest average salinity nearly corresponds to the time of highest sea level (dashed lines in Figure 8), however, the time of highest average salinity lags behind the time of highest sea level by an average of 15 ka in the late Pleistocene. This shows that the lag time in the shelf hydrologic system is longer in the late Pleistocene when sea level fluctuations are larger.

The magnitude of response to sea level forcing varies in the proximal and distal portions of the model. To illustrate this, we focus on two points through time within Unit 2 (Figure 9), proximal point P1 and distal point P2 (locations shown in Figure 6). Salinity with time at P1 has a large magnitude of change with each sea level cycle, ranging from 30 ppt during a sea level highstand to 10 ppt during a sea level lowstand (Figure 9a3). Salinity with time at P2 becomes fresher with each sea level cycle; however, the magnitude of change with each sea level cycle is <2 ppt from a sea level highstand to a sea level lowstand (Figure 9a3). The irregular salinity fluctuations (Figures 9a3, 9b3, and 9c3) under regular sea level fluctuations (Figures 9a1, 9b1, and 9c1) are the result of three-dimensional fluid flow and solute transport influenced by three-dimensional stratigraphic variability, most notably along-strike variations (Figures 2 and 7). Pore water samples offshore New Jersey also show complex salinity patterns in continental shelf sediments [*van Geldern et al*., 2013]. The magnitude of change in hydraulic head relative to change in sea level is similar in the proximal and distal points. The average hydraulic head of -20 to -30 m reflects the long-term trend of late Pleistocene sea level ranging from -120 to 0 m. The average shore-normal flow rates across distal and proximal near-surface sediments (Units 6 and 7) are similar. They are highest during sea level lowstands and reach up to 0.2 m/a.

5.2. Late Pleistocene Ice Sheets

To explore the effects of Pleistocene ice sheets, several models were run with sea level cycles (section 5.1) but also including an ice sheet boundary condition (Figure 5). When only simulating the LGM ice sheet (Figures 5b and 9b2), 35 km^3 of present-day freshwater offshore (2.2% of total fluid volume in the model domain) is predicted (Table 3). This is nearly double the amount of freshwater predicted in the simulation that only considered sea level change. The head induced by the LGM ice sheet drives freshwater 5 km farther offshore in the deeper sediments as compared to the sea level only simulation (Figure 6b). The salinity pattern beyond the maximum extent of the LGM, however, shows little difference from the sea level only simulation (Figures 6a, 6b, 7a, 7b, 9a3, and 9b3). The average salinity of the system is 23.5 ppt, <1 ppt lower then the sea level simulation (Table 3). These results are consistent with *Cohen et al*. [2010], who showed that glacially emplaced freshwater does not extend far beyond the edge of the LGM ice sheet.

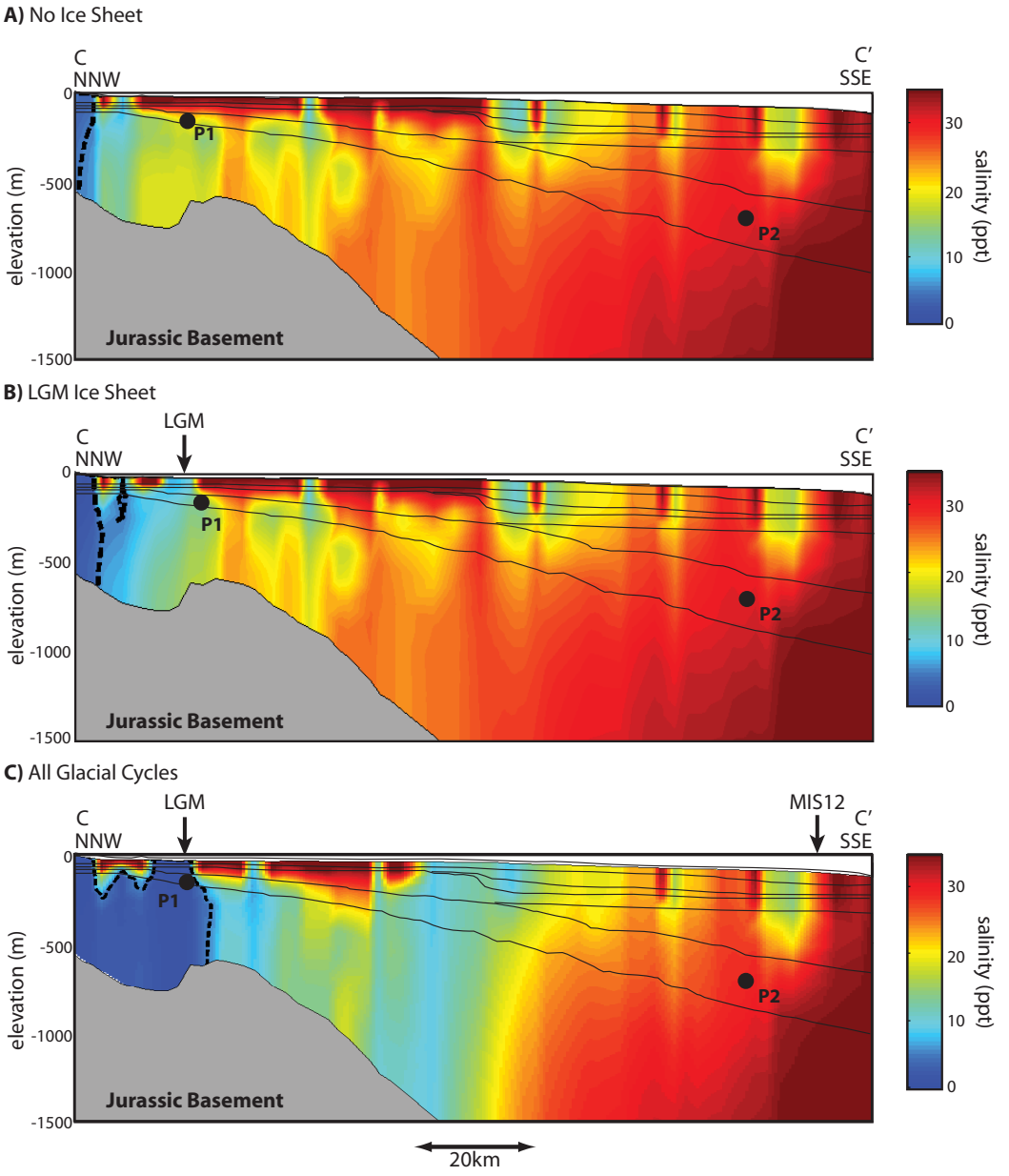

Figure 6. Predicted, present-day salinity for base-case model (Table 1) with sea level fluctuations shown in Figure 4 and (a) no ice sheet; (b) single ice sheet advance during the Last Glacial Maximum (LGM); and (c) ice advance during Marine Oxygen Isotope Stage (MIS) 12 followed by four additional ice advances to the margin of the LGM (all glacial cycles shown in Figure 5). Dashed black lines are 5 ppt salinity contour. Thin black lines mark model unit boundaries. Arrows indicate the maximum extents of the MIS 12 and LGM ice sheets. The black dots (P1 and P2) mark the locations where salinity and hydraulic head are displayed through time (see Figure 9). Location of cross sections is shown in Figure 3.

The MIS 12 ice sheet, followed by four additional late Pleistocene glacial cycles (all glacial cycles shown in Figure 5a) results in 100 km^3 of predicted, present-day freshwater offshore (6.3% of total fluid volume; Table 3). The freshwater extends up to 30 km beyond Martha's Vineyard (Figure 6c). This is more than 5 times as much freshwater than the sea level only simulation and almost 3 times as much freshwater than the LGM ice sheet simulation. The average salinity of the system is 19.3 ppt, and the shelf has a broad region of brackish water (5–30 ppt; Figure 6c).

5.3. Sensitivity Study

We conduct a sensitivity study to address the effects of permeability on freshwater distribution. Permeability has a strong control on the emplacement and preservation of Pleistocene meltwater in glaciated

Table 3. Results of Base-Case Model

Ice Boundary	Freshwater Volume (km^3)	Average Salinity (ppt)
No ice	18	24.2
LGM ice sheet	35	23.5
All glacial cycles	100	19.3

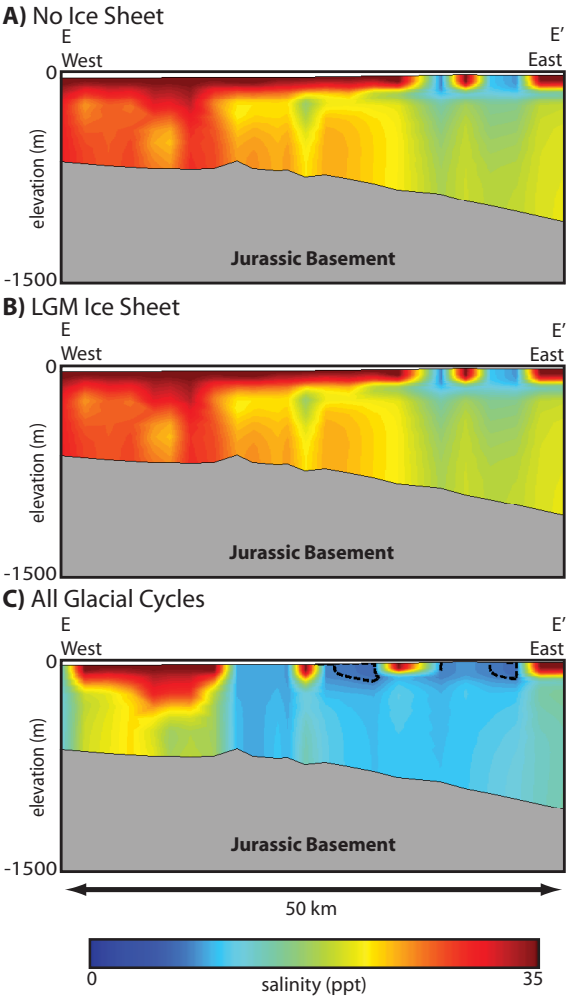

Figure 7. Predicted, present-day salinity for base-case model with sea level fluctuations shown in Figure 4 and (a) no ice sheet; (b) single ice sheet advance during the Last Glacial Maximum (LGM); and (c) ice advance during Marine Oxygen Isotope Stage (MIS) 12 followed by four additional ice advances to the margin of the LGM (all glacial cycles shown in Figure 5). Dashed black lines are 5 ppt salinity contour. Location of cross sections is shown in Figure 3.

sedimentary basins as low-permeability confining units prevent flushing of underlying aquifers after ice sheet retreat [*McIntosh et al.*, 2012; *Person et al.*, 2012]. Permeability was assigned to the base-case model based on lithology interpreted from seismic data. We, however, lack direct well control; therefore, there is uncertainty in our assigned lithology and permeability.

To evaluate the impact of permeability architecture on freshwater distribution, we ran models with different permeability (Table 4 and Figure 10). Sensitivity study 1 (SS1) tests the effects of a lower-permeability confining layer at the surface (Unit 7). Sensitivity study 2 (SS2) tests the effects of a higher-permeability carbonate aquifer (Unit 1). Sensitivity study 3 (SS3) tests a simplified lithology (alternating layers of high and low permeability), which resembles previous models [*Person et al.*, 2003; *Cohen et al.*, 2010]. We did not vary specific storage or porosity in our sensitivity studies. Specific storage, unlike permeability, does not vary by several orders of magnitude within continental shelf sediments and porosity, unlike permeability, does not have a first-order control on fluid flow.

5.3.1. Effect of Confining Unit Permeability at the Surface (SS1)

The lower-permeability confining unit at the surface (SS1) results in no predicted, present-day freshwater due to sea level change only. When considering sea level change and the LGM ice sheet, the model with the lower-permeability confining unit predicts 10 km^3 present-day freshwater offshore. Each of these volumes is less than predicted for the base-case model where the confining unit at the surface is more permeable (Tables 3–5). Less freshwater infiltration due to sea level change is expected, as the lower-permeability layer reduces vertical infiltration in the near-surface layer, and prevents freshwater from entering the system during sea level lowstands. *Cohen et al.* [2010] observed a similar pattern in their three-dimensional sensitivity study where including low-permeability confining layers resulted in the least volume of freshwater

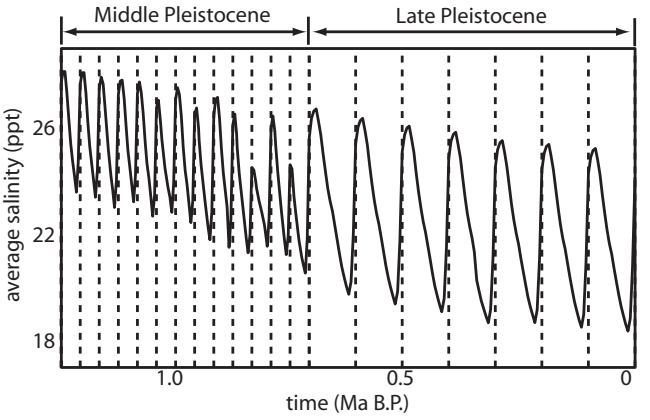

Figure 8. Average salinity for entire model domain from 1.25 Ma to present for base-case model (Table 1) with sea level fluctuations but no ice sheets. Dashed lines mark sea level highstands. Plot shows lag in response of subsurface hydrology to sea level inundation.

infiltration. Conversely, there is 109 km^3 of predicted, present-day freshwater from the MIS 12 and late Pleistocene glacial cycles (Table 5) with freshwater extending nearly as far as the base-case model (Figures 10a2 and 10b2). In this scenario, in the lower-permeability confining layer, the MIS 12 ice sheet produced a larger hydraulic head than the base-case model and the lateral head gradient at the base of the glacier also changes because of the elevation profile of the glacier (Figure 5). In addition, the glacial advance and retreat are asymmetric (Figure 9c2), which results in different times for the system to adapt to lateral flow during glacial advance and glacial retreat. Together these effects result in complex pressure and flow fields that change spatially and temporally. Consequently, even though the permeability is lower, freshwater infiltration occurs during glacial advances and this freshwater is driven laterally seaward. The lower-permeability layer helps preserve freshwater that was emplaced by the MIS 12 ice sheet by reducing the exfiltration rate of freshwater from all underlying units after ice sheet retreat (Figure 10b2).

5.3.2. Effect of Carbonate Permeability (SS2)

The inclusion of high-permeability carbonate sands without anisotropy (SS2) results in the emplacement of more freshwater under all boundary conditions compared to the base-case models. The predicted, present-day freshwater volume is 26, 58, and 104 km^3 from sea level change, the LGM, and the MIS 12 ice sheet boundary conditions (Table 5). There is only a small change, however, in the amount of freshwater for the late Pleistocene glaciation boundary condition as compared to the base-case model (Figures 10a2 and 10c2). The increase in stored freshwater is due to the high-permeability carbonate sands (Unit 1) which have an order of magnitude higher fluid velocity and, thus, more freshwater is advected offshore during sea level lowstands. This higher velocity coupled with no anisotropy results in more dispersive mixing in the carbonate sands which smoothes the salinity gradient in the carbonate sands but also moves the 5 ppt salinity contour landward in comparison to the base-case model (Figures 10a2 and 10c2).

5.3.3. Effect of Simplified Lithology (SS3)

The simplified lithology (SS3) of alternating layers of high permeability (10^{-14} m^3) and low permeability (10^{-16} m^3) results in the smallest volume of freshwater in the system after the MIS 12 and late Pleistocene glaciations. The predicted, present-day freshwater volume with the MIS 12 ice sheet boundary conditions is 70 km^3 (Table 5), with the maximum extent being 25 km offshore (Figure 10d2). This difference is primarily due to the lack of a large carbonate aquifer (Unit 1) that the previous models had and which enhances recharge of glacially derived freshwater.

5.4. Extended Ice Sheet Scenario

The difference in predicted freshwater between the base-case model with all the glacial cycles, including the MIS 12 ice sheet, and the base-case model with the LGM ice extent is likely due to (1) enhanced freshwater infiltration, where compared to the LGM ice sheet, the MIS 12 ice sheet was thicker (i.e., a larger driving force) and had a more expansive areal extent (i.e., a larger region affected by glacial recharge) and (2) remnant overpressure (hydraulic head in excess of hydrostatic) after the MIS 12 ice sheet retreat. Remnant pressures are created because of the interplay of asymmetric glacial loading, enhanced recharge driven by high pressures at the base of the glaciers in space and time, and lateral pressure transfer in permeable layers bounded by lower-permeability layers. This process is similar to lateral pressure transfer or flow focusing described in clay-sand systems [e.g., *Yardley and Swarbrick*, 2000; *Flemings et al*., 2002] where regions with high overpressure due to rapid, asymmetric sediment loading transmit overpressure to regions where

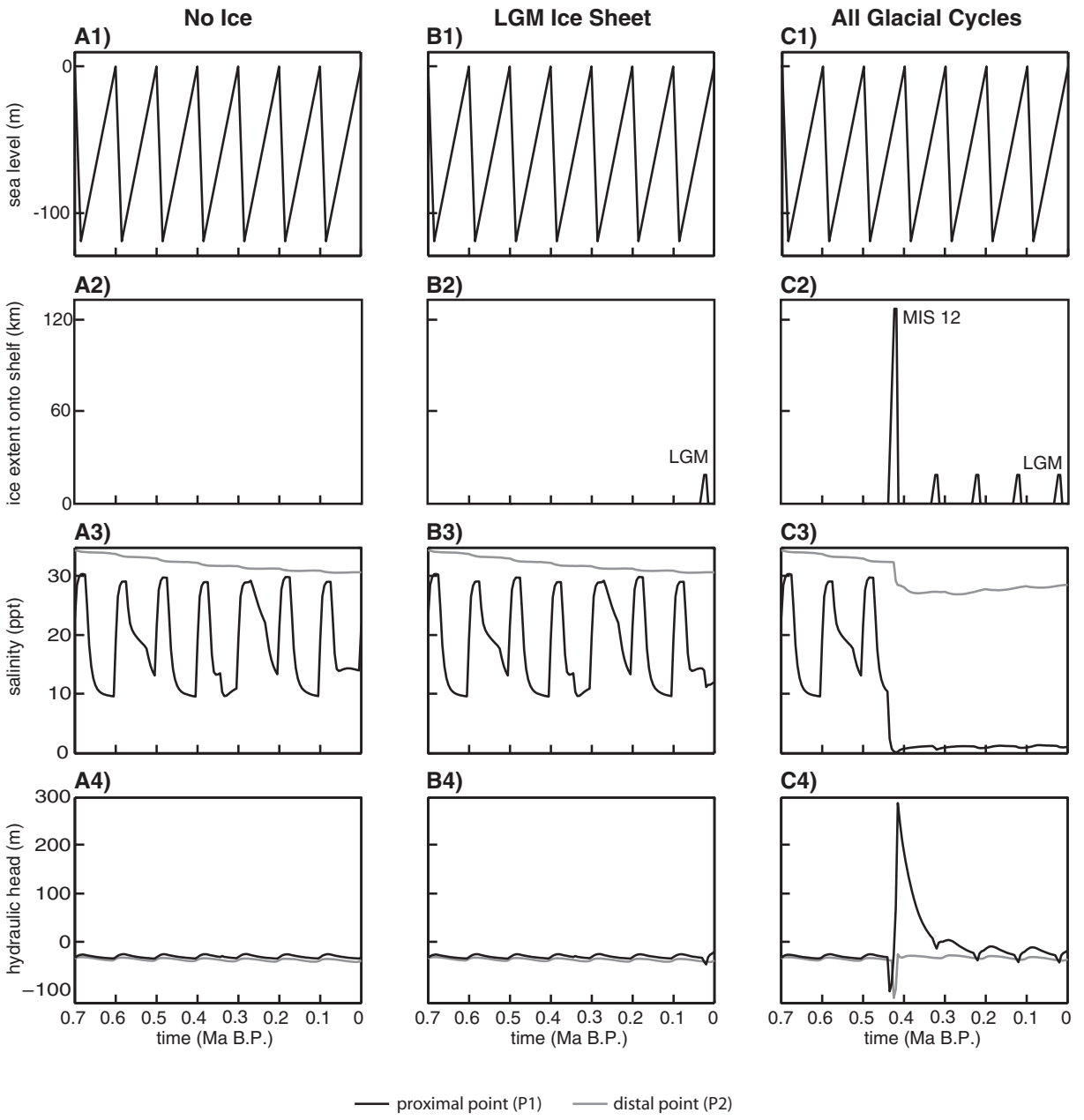

Figure 9. (a1, b1, and c1) Late Pleistocene sea level curve used in all models. Ice sheet extent onto shelf used for boundary conditions of (a2) no ice; (b2) LGM ice sheet; and (c2) all five glacial cycles. (a3, b3, and c3) Salinity and (a4, b4, and c4) hydraulic head through time at a specific proximal point (P1) and distal point (P2) within Unit 2 (carbonate mud) for the specific boundary conditions of sea level and ice sheets shown above. Time series for the proximal point (P1) is shown in black and the time series for the distal point (P2) is shown in gray. Figure 6 shows the location of the two analysis points.

loading was less. In our model system, the glaciers provide the asymmetric load and elevated heads at the base of the glacier, which drive lateral flow. This result is time dependent as the glacier advances/retreats over time. Retreat of the glacier decreases pressures due to unloading [e.g., *Neuzil*, 1993]; however, it is after some loading-induced lateral pressure transfer. This creates a complex pattern of pressure generation, pressure transfer, and pressure decrease in three dimensions. We focus on the key results of this asymmetric loading-unloading and flow system for the MIS 12 glacial advance and subsequent glaciations.

There is an order of magnitude increase in freshwater infiltration during the MIS 12 glacial advance to near the shelf-slope break. Freshwater was emplaced throughout the shelf with 376 km^3 of emplaced freshwater by the time the ice sheet reaches its maximum extent (425 ka B.P.). This is consistent with continental-scale

Table 4. Horizontal Permeability (m^2) Used for Sensitivity Studies[a]

Unit	Lithology	BC	SS1	SS2	SS3
7	Glacial outwash	10^{-13}	10^{-16}	10^{-13}	10^{-16}
6	Sand, silt, clay clinoforms	10^{-15}	10^{-15}	10^{-15}	10^{-14}
5	Thin clay layer	10^{-17}	10^{-17}	10^{-17}	10^{-14}
4	Glacigenic sediments	10^{-15}	10^{-15}	10^{-15}	10^{-16}
3	Silt/clay clinoforms	$10^{-17}/10^{-14}/10^{-17}$	$10^{-17}/10^{-14}/10^{-17}$	$10^{-17}/10^{-14}/10^{-17}$	10^{-14}
2	Carbonate mud	10^{-15}	10^{-15}	10^{-15}	10^{-14}
1	Carbonate sandstone	10^{-14}	10^{-14}	10^{-13b}	10^{-16}

[a]Anisotropy: vertical/horizontal permeability (k_z/k_x) = 0.1.
[b]No anisotropy.

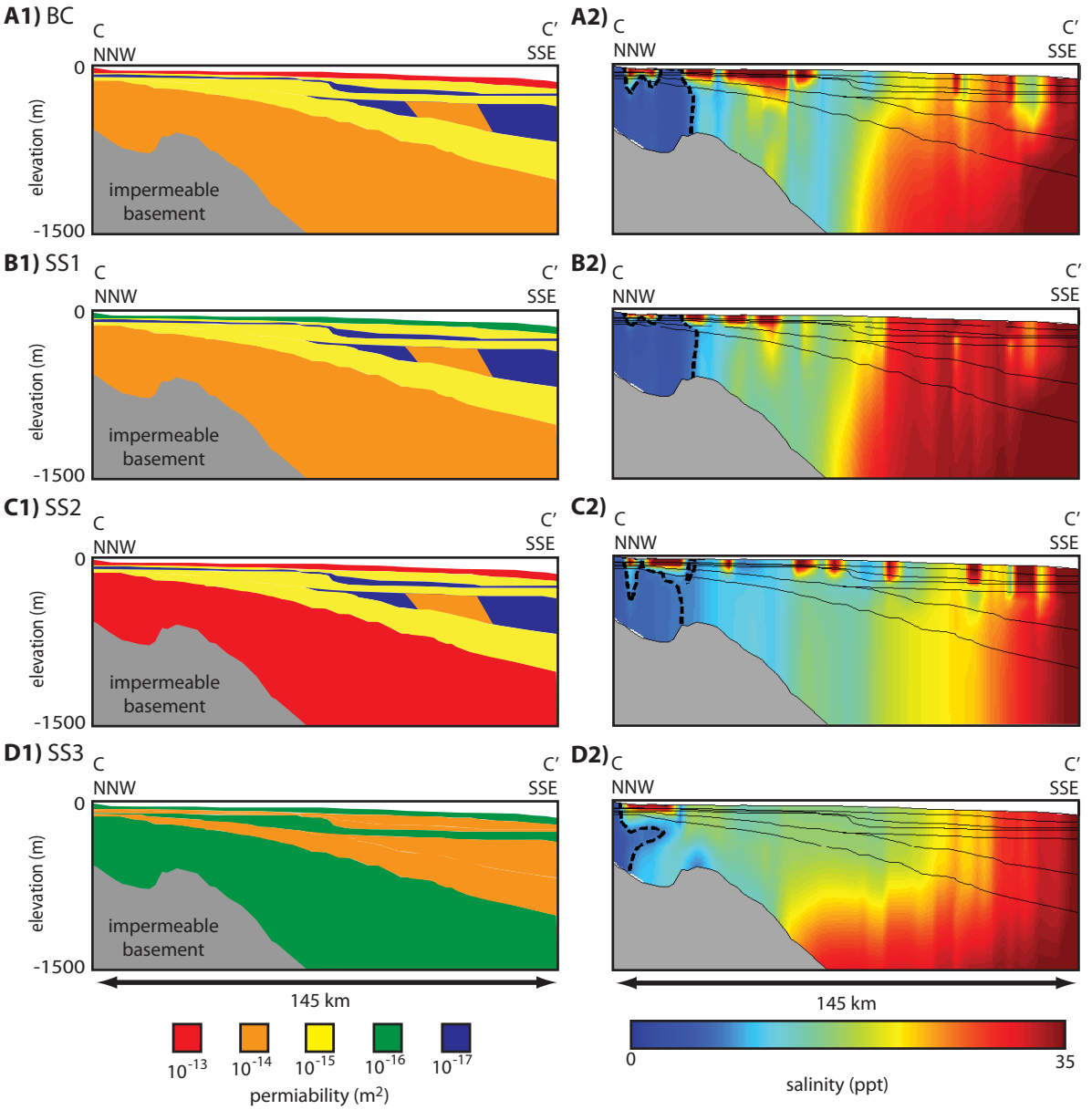

Figure 10. Results of base-case model and sensitivity tests (Tables 1 and 4). (a1, b1, c1, and d1) The permeability assigned to each model unit. (a2, b2, c2, and d2) The corresponding, present-day salinity after sea level change and all five glacial cycles. The dashed black lines show location of 5 ppt salinity contour. Thin black lines mark model unit boundaries. Location of cross section (C–C′) is shown in Figure 3. Figures 10a1 and 10a2 are base-case model results. Figures 10b1 and 10b2 are effect of confining unit permeability at the surface (SS1). Figures 10c1 and 10c2 are effects of carbonate permeability (SS2). Figures 10d1 and 10d2 are effect of simplified lithology (SS3).

Table 5. Freshwater Volume in Sensitivity Studies (km^3)

Ice Boundary	SS1	SS2	SS3
No ice	0.0	26	18
LGM ice sheet	10	58	55
All glacial cycles	109	104	70

models of the Laurentide ice sheet, where ice sheet loading produces large volumes of freshwater that infiltrate and charge deep basins [*Lemieux et al*., 2008a]. The four late Pleistocene glacial cycles following the MIS 12 glaciation each recharge several 10s of km^3 of freshwater into the system; however, our analysis suggests the majority of the freshwater offshore at present was emplaced by the MIS12 ice sheet. *Lemieux et al*. [2008a] noted that permafrost could influence freshwater infiltration rate as it creates an impermeable layer at the surface. We did not include the formation of permafrost because of the proximity to the ocean which we track during our prescribed sea level cycles. This proximity to the ocean moderates the temperature, and we assumed this would keep it above freezing and, thus, prevent the formation of sustained permafrost regions.

MIS 12 ice sheet loading and pressures at the base of the glacier cause an increase in overpressure in the permeable sediments above Unit 5. The overpressure decreases to the south as ice thickness decreases, and consequently, creates a seaward overpressure gradient that yields increased seaward-directed fluid flow in shelf sediments. This drives freshwater offshore. *McIntosh et al*. [2011] predicted a similar pattern in the near-surface sediments of the Michigan basin during glaciations, which contributed to freshwater flushing of sedimentary units below and beyond the extent of the Laurentide ice sheet.

Overpressures that develop due to the MIS 12 ice sheet are preserved below low-permeability confining layers (Units 3 and 5) long after ice sheet retreat (400 Ka B.P.; Figures 9c4, 11a, and 11b). When the MIS 12 ice sheet was at its maximum (425 ka B.P.), nearly 1000 m of excess hydraulic head developed in the sediment where ice overburden was greatest (see Figure 5b for MIS 12 ice sheet profile). By the time the ice sheet has fully retreated and sea level is at a highstand (400 ka B.P.), overpressure in sediments above the

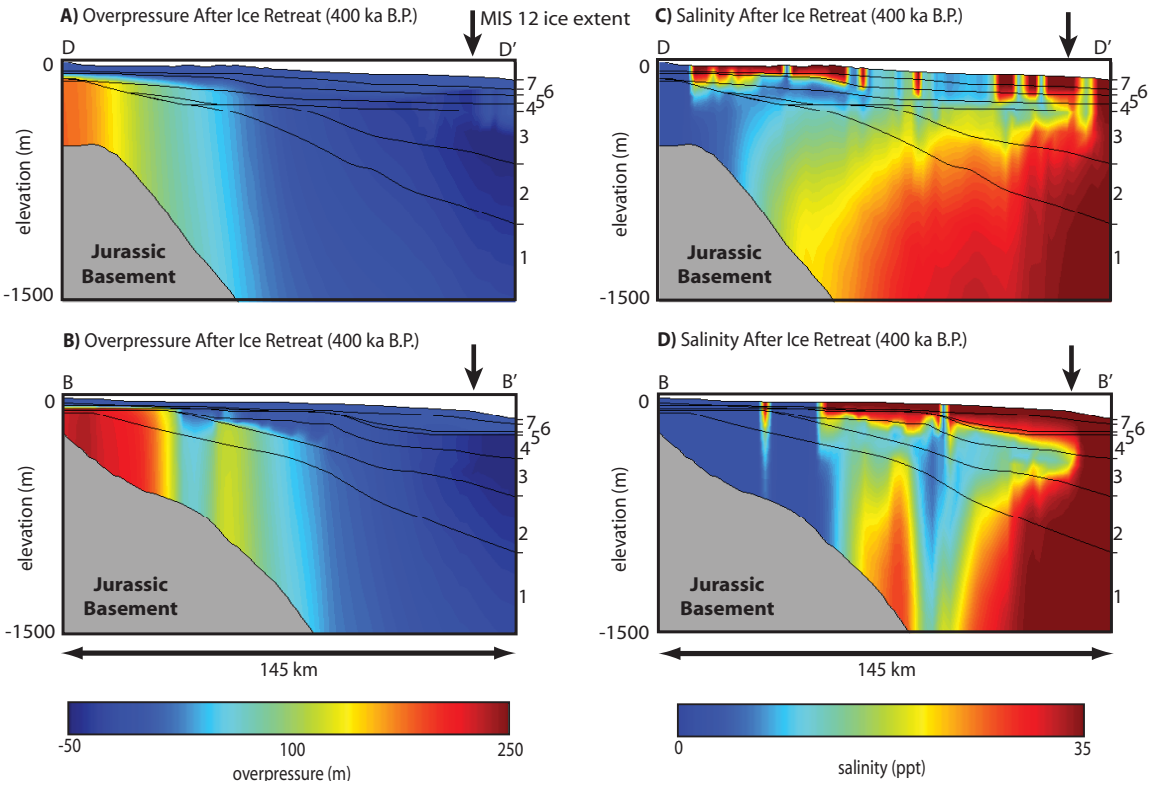

Figure 11. (a and b) Overpressure immediately after MIS 12 ice sheet retreat (400 ka B.P.) for cross sections D–D′ and B–B′. Most of the overpressure is below Unit 3, a low-permeability clinoform layer. (c and d) Salinity after MIS 12 ice sheet retreat (400 ka B.P.) for cross sections D–D′ and B–B′. Black lines mark model stratigraphy. Lithologic unit numbers are identified on the right of each image. Units 3 and 5 have a low-permeability clinoform. Location of cross sections D–D′ (Figures 11a and 11b) and B–B′ (Figures 11c and 11d) are shown in Figure 3.

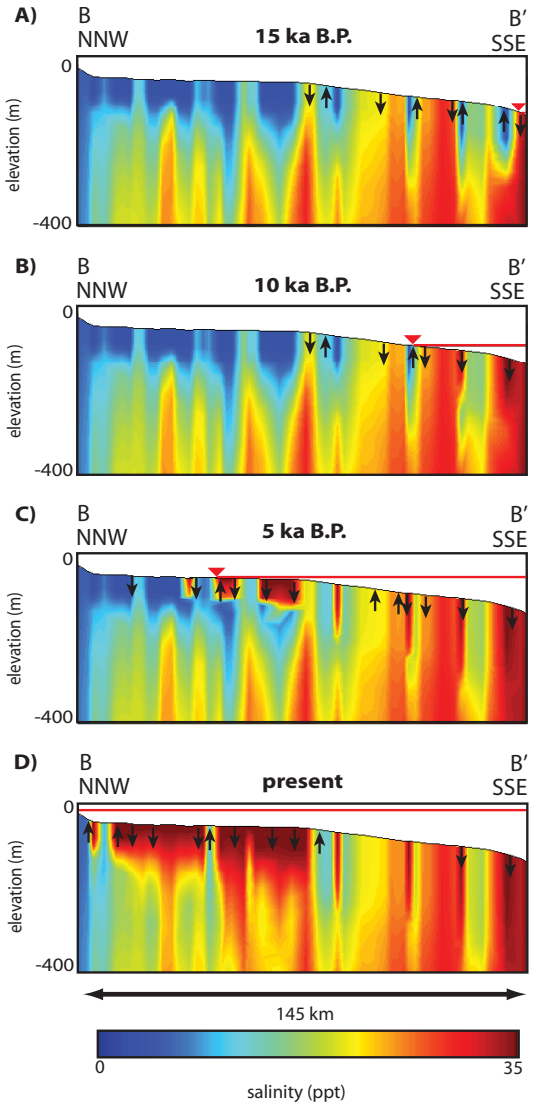

Figure 12. Salinity profiles of near-surface sediments during sea level rise at (a) 15 ka B.P., (b) 10 ka B.P., (c) 5 ka B.P., and (d) present. Arrows mark the direction of vertical fluid flow. The red lines mark sea level and the red triangles mark the shoreline location. Location of cross section B–B′ is shown in Figure 3.

confining layers has nearly dissipated and hydraulic head is equivalent to sea level (Figures 11a and 11b). Sediments below the confining layers, however, maintain elevated overpressure after the ice sheet has fully retreated (Figures 11a and 11b). This occurs from the migration of overpressure into the deeper sediments during MIS 12 ice sheet retreat. *McIntosh et al*. [2011] observed a similar phenomenon of glacially derived overpressure persisting in deeper confining units in their model after ice sheet retreat.

Remnant, glacially derived overpressure helps preserve emplaced freshwater because the overpressure drives fluid flow toward the surface, and thus, prevents downward intrusion of seawater during highstands. Remnant overpressure is higher in the northwest region (landward portion Figure 11b) of the model because the northwest region (landward portion of Figure 11b) contains a thicker section of a low-permeability clinoform in Unit 3 as compared to the northeastern region (landward portion of Figure 11a). The difference in remnant overpressure results in a different salinity pattern where the northwestern region has more freshwater and a greater offshore extent of freshwater compared to the northeastern region (Figures 11c and 11d).

The results of the sensitivity studies in our analyses further highlight the important effect of an extensive MIS 12 ice sheet for the emplacement of a large volume of freshwater offshore Massachusetts. In all three sensitivity studies, the addition of the MIS 12 ice sheet increased the amount of offshore freshwater (Table 5). For SS1 and SS2, the predicted extent of freshwater from the MIS 12 ice sheet at present is primarily contained within 30 km of Martha's Vineyard (Figures 10b2 and 10c2). This is similar to the base-case model (Figure 10a2). This volume of freshwater is twice as much as predicted based on a simplified lithology (SS3) and as predicted based on the LGM ice sheet extent only (Table 5). Thus, our knowledge of an extensive MIS 12 ice sheet and our improved three-dimensional model geometry allow us to better constrain probability for a relatively large volume of nonrenewable freshwater to exist offshore Massachusetts.

5.5. Seafloor Topography and Sea Level Change

Seafloor topography (elevation and relief) has a direct control on the infiltration of freshwater and the distribution of the mixing zone between freshwater and salt water because (1) seafloor elevation determines exposure during a lowstand, where a lowstand exposes the shelf to increased meteoric recharge [*Meisler et al*., 1984] and (2) seafloor relief controls the rate of shoreline transgression during sea level rise, where rapid transgression leads to density instabilities (high-density salt water overlying low-density freshwater) that lead to advection and a broad zone of brackish water [*Kooi et al*., 2000]. In simple, cross-sectional

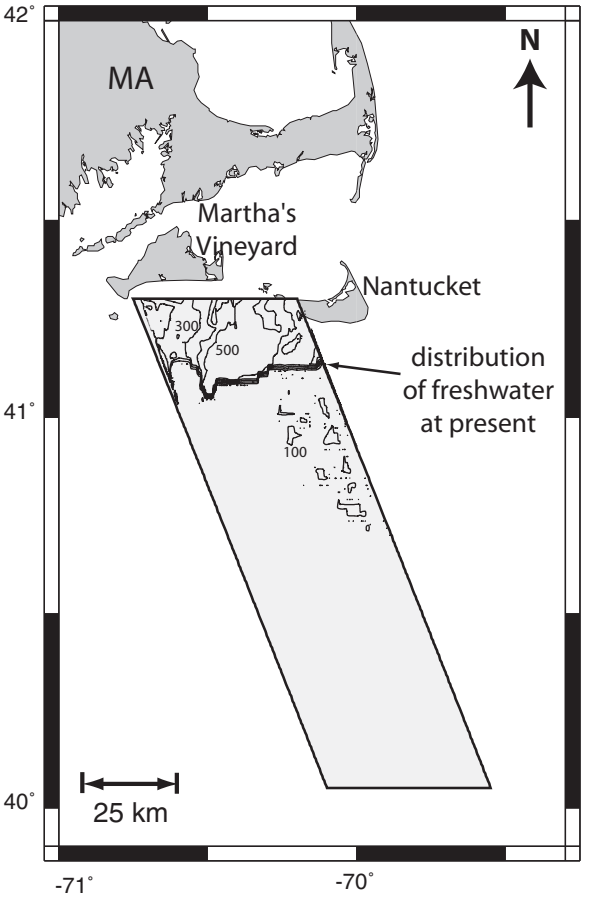

Figure 13. Plan view of predicted, present-day freshwater distribution for the base-case model after sea level change and all five glacial cycles. Contours are thickness in meters of the continental shelf sediments that contain freshwater. The model domain is marked with the thick black lines and shaded light gray.

numerical models, these processes proved effective at emplacing freshwater and creating broad zones of brackish water offshore. In our three-dimensional model, however, we observe these processes occurring in the north-south (downdip/shore-normal) and east-west (along-strike/shore-parallel) directions because of variations in the three-dimensional seafloor elevation of 20 m across the northern section of the model (Figures 3 and 7). For the base-case model with sea level change only, freshening of the sediments occurs for a longer period of time on the northeastern side of the model during each sea level lowstand, and consequently the northeastern side of the model contains fresher water (Figure 7a).

The east-west difference in elevation across the model domain also results in different average salinity across the region that experienced ice sheet loading (Figure 7c). The eastern half of the model has an average salinity of 10.1 ppt and the western half has an average salinity of 18.6 ppt, even though the cross section experienced the same magnitude of ice sheet loading. This further shows that topography has a strong control on the freshwater distribution. Previous, two-dimensional, cross-section models were not able to explore the subtle effects of seafloor elevation on freshwater distribution after glaciations.

Seafloor topography also affects the distribution of freshwater in near-surface sediments (Units 6 and 7) as it engenders convection cells up to tens of kilometers in length and up to 100s of meters in depth that redistribute fresh and saline water (Figure 12). The convection cells develop from density differences that are a direct result of the seafloor topography. Seafloor relief causes isotherms in the near-surface sediments to dip (i.e., they parallel the seafloor), which can induce thermally derived density differences and convection in high-permeability ($>10^{-15}$ m^2) sediments [*Wilson and Ruppel*, 2007]. For that reason, convection cells do not develop in the sensitivity test (SS1), which contains a low-permeability layer at the surface (Figures 10a1 and 10a2). Seafloor elevation controls shelf exposure time, where sea level lowstands cause dense saline water to move downward, which can induce salinity-derived density instabilities and convection [*Kooi et al*., 2000]. For that reason, we observe convection cells on the exposed portion of the shelf (Figures 12a and 12b).

The convection cells in the base-case model develop periodically across the model space both above and below sea level; however, they are more numerous when the shelf is inundated. The periodic development of the convection cells in the upper sediment layers affects the freshwater distribution in two ways: (1) during a sea level lowstand, there are regions of the model with subaerial surface nodes that are not freshening as fluid is being discharged in these areas and, therefore, freshwater cannot infiltrate and (2) during a sea level highstand, there are previously freshened regions of the model with subaqueous surface nodes that are not becoming more saline as fluid is being discharged in these areas and seawater cannot infiltrate. This suggests that areas of high-permeability offshore may have freshwater that was emplaced during a sea level lowstand and preserved as convection cells that developed subsequently during a sea level highstand prevented the infiltration of seawater into the sediments.

5.6. Current Freshwater Distribution

The discovery of an MIS 12 glaciation that extended to near the shelf-slope break suggests that there is an increased likelihood of freshwater far offshore Massachusetts; however, three-dimensional variation in seafloor elevation and the three-dimensional distribution of stratigraphy (clinoform confining units and carbonate sands) strongly influenced the emplacement and distribution of freshwater through time. Most of the present-day freshwater is in the northern section of the model domain within 30 km of Martha's Vineyard (Figure 13). This freshwater is distributed in a complex pattern influenced by the stratigraphy and the history of sea level and glaciations. *van Geldern et al.* [2013] observed complex salinity patterns within continental shelf sediments offshore New Jersey that are qualitatively similar to those we simulate. In addition, subtle differences in seafloor elevation resulted in more freshwater on the eastern half of the model than the western half (Figure 13), even though there was more freshwater in the western half of the model after the MIS 12 ice sheet retreat (Figure 11). Three-dimensional ice sheet thickness was not explored. Due to the effects of ice sheet gradient on subsurface fluid flow, we infer that the three-dimensional ice sheet thickness would also have an impact on freshwater emplacement and distribution. Future studies, including offshore drilling or electromagnetic surveys, could provide critical data to improve our understanding of the complex relationship between three-dimensional shelf stratigraphy, three-dimensional seafloor topography, and three-dimensional ice sheet growth. A better understanding of the freshwater distribution and dynamics may help constrain (1) the generation of microbial methane [*Martini et al.*, 1998; *Schlegel et al.*, 2011]; (2) the availability of freshwater resources [*Kooi and Groen*, 2003; *Person et al.*, 2007a; *Post et al.*, 2013]; (3) submarine groundwater discharge and the nutrient supply to the ocean over time [*Slomp and Cappellen*, 2004]; and (4) the safety and long-term storage of nuclear waste [*Iverson and Person*, 2012; *Vidstrand et al.*, 2013].

6. Conclusions

Three-dimensional, variable-density, numerical modeling that couples fluid flow and heat and solute transport on the continental shelf offshore Massachusetts provides evidence that the extent and duration of ice sheet advance on the continental shelf impacts freshwater emplacement volumes in the continental shelf. In our modeled system, an MIS 12 ice sheet followed by four late Pleistocene glacial cycles resulted in as much as 100 km^3 of present-day freshwater offshore (base case, sensitivity study 1, and sensitivity study 2 models). Most of the freshwater ($<$5 ppt salinity) is within 30 km of Martha's Vineyard and shallower than 500 mbsl. Sensitivity studies that address permeability also show that the MIS 12 ice sheet resulted in significantly larger volumes of freshwater (70–109 km^3) as compared to models that only included the LGM ice sheet (35–58 km^3) and models that did not include ice sheets (0–26 km^3). We demonstrate that more freshwater exists offshore than previously estimated; this is due to better constraints of the glacial history and inclusion of detailed three-dimensional topography and lithology. Additional constraints on ice sheet extent, duration, and size and on physical properties of shelf sediments may help refine emplaced freshwater volumes. New observations, either direct with drilling and sampling or interpretation via electromagnetic methods, however, are required to provide tests of these models. Accurate emplacement volumes are valuable as the freshwater that exists offshore is an important, nonrenewable resource for Massachusetts's coastal communities, however, geochemical data are needed to further determine the distribution of the freshwater and to fully address its utility as a resource.

Acknowledgments

This work was funded by NSF-OCE-0824368. Seismic data were collected on the R/V Endeavor (cruise EN465) using Scripps Institution of Oceanography's portable seismic system. All seismic data are available from the Marine Geoscience Data System (http://www.ig.utexas.edu/sdc/). Original model input and output files can be requested by contacting Brandon Dugan (dugan@rice.edu). We thank the Scripps technicians and the crew of the R/V Endeavor for their assistance in collecting the data. This paper benefited from constructive comments by Tom McKenna and one anonymous reviewer.

References

Balco, G., and C. W. Rovey II (2010), Absolute chronology for major Pleistocene advances of the Laurentide Ice Sheet, *Geology*, *38*(9), 795–798.

Barlow, P. M. (2003), Ground water in freshwater-saltwater environments of the Atlantic Coast, *U.S. Geol. Surv. Circ.*, *1262*, 1–113.

Bense, V. F., and M. A. Person (2008), Transient hydrodynamics within intercratonic sedimentary basins during glacial cycles, *J. Geophys. Res.*, *113*, F04005, doi:10.1029/2007JF000969.

Bintanja, R., and R. S. W. van de Wal (2008), North American ice sheet dynamics and the onset of 100,000-year glacial cycles, *Nature*, *454*, 869–872.

Boulton, G. S., and P. Caban (1995), Groundwater flow beneath ice sheets: Part II—Its impact on glacier tectonic structures and moraine formation, *Quat. Sci. Rev.*, *14*, 563–587.

Cohen, D., et al. (2010), Origin and extent of fresh paleowaters on the Atlantic continental shelf, USA, *Ground Water*, *48*(1), 143–158.

de Marsily, G. (1986), *Quantitative Hydrogeology, Groundwater Hydrology for Engineers*, Academic, N. Y.

DeFoor, W. (2011), Paleo-hydrogeologic models of freshwater emplacement on the Atlantic continental shelf: Offshore Martha's Vineyard Island, MS thesis, N. M. Inst. of Min. and Technol. Socorro, N. M.

Ferguson, G., and T. Gleeson (2012), Vulnerability of coastal aquifers to groundwater use and climate change, *Nat. Clim. Change*, *2*, 342–345.

Flemings, P., B. Stump, T. Finkbeiner, and M. Zoback (2002), Flow focusing in overpressured sandstones: Theory, observations, and applications, *Am. J. Sci.*, *302*(10), 827–855, doi:10.2475/ajs.302.10.827.

Folger, D. W., J. C. Hathaway, R. A. Christopher, P. C. Valentine, and C. W. Poag (1978), Stratigraphic test well, Nantucket Island, Massachusetts, *U.S. Geol. Surv. Circ.*, *773*, 1–28.

Freeze, R. A., and J. A. Cherry (1979), *Groundwater*, Prentice Hall, Englewood Cliffs, N. J.

Gable, C. W., H. E. Trease, and T. A. Cherry (1996), Geological applications of automatic grid generation tools for finite elements applied to porous flow modeling, in *Numerical Grid Generation in Computational Fluid Dynamics and Related Fields*, pp. 1007–1015, Mississippi State University Press, Starkville, Miss.

Hathaway, J. C., C. W. Poag, P. C. Valentine, R. E. Miller, D. M. Schultz, F. T. Manheim, F. A. Kohout, M. H. Bothner, and D. A. Sangrey (1979), U.S. Geologic Survey core drilling on the Atlantic shelf, *Science*, *206*(4418), 515–527.

Huybers, P. (2007), Glacial variability over the last two million years: An extended depth-derived age model, continuous obliquity pacing, and the Pleistocene progression, *Quat. Sci. Rev.*, *26*, 37–55.

Imbrie, J., J. Hays, D. Martinson, A. McIntyre, A. C. Mix, J. Morley, N. G. Pisias, W. L. Prell, and N. J. Shackleton (1984), The orbital theory of Pleistocene climate: Support from a revised chronology of the marine δ^{18}O record, in *Milankovitch and Climate*, pp. 269–305, D. Reidel, Boston, Mass.

Ingebritsen, S., W. Stanford, and C. Neuzil (2007), *Groundwater in Geologic Processes*, Cambridge Univ. Press, N. Y.

Iverson, N., and M. Person (2012), Glacier-bed geomorphic processes and hydrologic conditions relevant to nuclear waste disposal, *Geofluids*, *12*(1), 38–57.

Kestin, J., H. E. Khalifa, and R. Corriea (1981), Tables of the dynamics and kinematic viscosity of aqueous NaCl solutions in the temperature range of 20–150°C and the pressure range of 0.1–35 MPa, *J. Phys. Chem. Ref. Data*, *10*, 71–87.

Kohout, F. A., J. C. Hathaway, D. W. Folger, M. H. Bothner, E. H. Walker, D. F. Delaney, M. H. Frimpter, E. G. A. Weed, and E. V. C. Rhodehamel (1977), Fresh groundwater stored in aquifers under the continental shelf, implications from a deep test, Nantucket Island, Massachusetts, *Water Resour. Bull.*, *13*(2), 373–386.

Kohout, F. A., H. Meisler, F. W. Meyer, R. H. Johnston, G. W. Leve, and R. L. Wait (1988), Hydrogeology of the Atlantic continental margin, in *The Atlantic Continental Margin: U. S.*, edited by R. E. Sheridan and J. A. Grow, pp. 463–480, The Geol. Soc. of Am., Boulder, Colo.

Konikow, L. F., and D. B. Grove (1977), Derivation of equations describing solute transport in groundwater, *U. S. Geol. Surv. Water Resour. Invest.*, 77–19.

Kooi, J., and J. Groen (2003), Geological processes and the management of groundwater resources in coastal areas, *Neth. J. Geosci*, *82*(1), 31–40.

Kooi, H., J. Groen, A. Leijnse (2000), Modes of seawater intrusion during transgressions, *Water Resour. Res.*, *36*(12), 3581–3589.

Lambe, T. W., and R. V. Whitman (1969), *Soil Mechanics*, John Wiley, N. Y.

Lemieux, J. M., E. A. Sudicky, W. R. Peltier, and L. Tarasov (2008a), Dynamics of groundwater recharge and seepage over the Canadian landscape during the Wisconsinian glaciation, *J. Geophys. Res.*, *113*, F01011, doi:10.1029/2007JF000838.

Lemieux, J. M., E. A. Sudicky, W. R. Peltier, and L. Tarasov (2008b), Simulating the impact of glaciations on continental groundwater flow systems: 1. Relevant processes and model formulation, *J. Geophys. Res.*, *113*, F03017, doi:10.1029/2007JF000928.

Lisiecki, L. E., and M. E. Raymo (2005), A Pliocene-Pleistocene stack of 57 globally distributed benthic δ^{18}O records, *Paleoceanography*, *20*, PA1003, doi:10.1029/2004PA001071.

Lisiecki, L. E., and M. E. Raymo (2007), Plio-Pleistocene climate evolution: Trends and transitions in glacial cycle dynamics, *Quat. Sci. Rev.*, *26*, 56–69.

Marksamer, A. J., M. Person, F. Day-Lewis, J. W. Lane, D. Cohen, B. Dugan, H. Kooi, and M. Willett (2007), Integrating geophysical, hydrochemical, and hydrologic data to understand the freshwater resources on Nantucket Island, Massachusetts, in *Subsurface Hydrology Data Integration in Subsurface Hydrology: Data Integration for Properties and Processes, Geophys. Monogr. Ser.*, vol. 171, edited by D. W. Hyndman, F. D. Day-Lewis, and K. Singha, pp. 143–159, AGU, Washington, D. C.

Marshall, S. J., T. S. James, and G. K. C. Clark (2002), North American ice sheet reconstructions at the Last Glacial Maximum, *Quat. Sci. Rev.*, *21*, 175–192.

Martini, A. M., L. M. Walter, J. M. Budai, T. C. W. Ku, C. J. Kaiser, and M. Schoell (1998), Genetic and temporal relations between formation waters and biogenic methane: Upper Devonian Antrim Shale, Michigan Basin, USA, *Geochim. Cosmochim. Acta*, *62*(10), 1699–1720.

McIntosh, J. C., and L. M. Walter (2005), Volumetrically significant recharge of Pleistocene glacial meltwaters into epicratonic basins: Constraints imposed by solute mass balances, *Chem. Geol.*, *222*, 292–309.

McIntosh, J. C., G. Garven, and J. S. Hanor (2011), Impacts of Pleistocene glaciation on large-scale groundwater flow and salinity in the Michigan Basin, *Geofluids*, *11*, 18–33.

McIntosh, J. C., M. E. Schlegel, and M. Person (2012), Glacial impacts on hydrologic processes in sedimentary basins: Evidence from natural tracer studies, *Geofluids*, *12*, 7–21.

Meisler, H., P. P. Leahy, and L. L. Knobel (1984), Effects of Eustatic Sea-level changes on saltwater-freshwater relations in the Northern Atlantic coastal plain, *U.S. Geol. Surv. Water Supply Pap.*, *2255*, 1–28.

Metzger, J. M., P. B. Flemings, N. Christie-Blick, G. S. Mountain, J. A. Austin Jr., and S. P. Hesselbo (2000), Late Miocene to Pleistocene sequences at the New Jersey outer continental shelf (ODP leg 174A, sites 1071 and 1072), *Sediment. Geol.*, *134*, 149–180.

Morrissey, S. K., J. F. Clark, M. Bennett, E. Richardson, and M. Stute (2010), Groundwater reorganization in the Floridan aquifer following Holocene sea-level rise, *Nat. Geosci.*, *3*, 683–687.

Neuzil, C. E. (1993), Low fluid pressure within the Pierre Shale: A transient response to erosion, *Water Resour. Res.*, *29*(7), 2007–2020.

Neuzil, C. E. (2012), Hydromechanical effects of continental glaciation on groundwater systems, *Geofluids*, *12*(1), 22–37.

Oldale, R. N., and C. J. O'Hara (1984), Glaciotectonic origin of the Massachusetts coastal end moraines and a fluctuating late Wisconsinan ice margin, *GSA Bull.*, *95*, 61–74.

Peltier, W. R. (2011), Long-term climate change, *Tech. Rep. DGR-TR-2011-14*, p. 101, Nucl. Waste Manage. Organ, Toronto, Canada.

Peltier, W. R. and J. T. Andrews (1976), Glacial-Isostatic adjustment—I. The forward problem, *Geophys. J. R. Astron. Soc.*, *46*, 605–646.

Person, M., B. Dugan, J. Swenson, L. Urbano, C. Stott, J. Taylor, and M. Willett (2003), Pleistocene hydrogeology of the Atlantic continental shelf, New England, *Geol. Soc. Am. Bull.*, *115*, 1324–1343.

Person, M., J. McIntosh, V. Bense, and V. H. Remenda (2007a), Pleistocene hydrology of North America: The role of ice sheets in reorganizing groundwater flow systems, *Rev. Geophys.*, *45*, RG3007, doi:10.1029/2006RG000206.

Person, M., P. Roy, H. Wright, W. Gutowski Jr., E. Ito, T. Winter, D. Rosenberry, and D. Cohen (2007b), Hydrologic response of the Crow Wing Watershed, Minnesota, to mid-Holocene climate change, *GSA Bull.*, *119*(3/4), 363–376.

Person, M., V. Bense, D. Cohen, and A. Banerjee (2012), Models of ice-sheet hydrogeologic interactions: A review, *Geofluids*, *12*(1), 58–78.

Piper, D. J. W., P. J. Mudie, A. E. Aksu, K. I. and Skene (1994), A 1 Ma record of sediment flux south of the Grand Banks used to infer the development of glaciation in southeastern Canada, *Quat. Sci. Rev.*, *13*, 23–37.

Post, V. E. A., J. Groen, H. Kooi, M. Person, S. Ge, and W. M. Edmunds (2013), Offshore fresh groundwater as a global phenomenon, *Nature*, *504*, 71–78, doi:10.1038/nature12858.

Ruddiman, W. F., M. Raymo, and A. McIntyre (1986), Matuyama 41,000-year cycles: North Atlantic Ocean and northern hemisphere ice sheets, *Earth Planet. Sci. Lett.*, *80*, 117–129.

Schlegel, M. E., Z. Zhou, J. C. McIntosh, C. J. Ballentine, and M. A. Person (2011), Constraining the timing of microbial methane generation in organic-rich shale using noble gases, Illinois Basin, USA, *Chem. Geol.*, *287*, 27–40.

Siegel, J., B. Dugan, D. Lizarralde, M. Person, W. DeFoor, and N. Miller (2012), Geophysical evidence of a late Pleistocene glaciation and paleo-ice stream on the Atlantic Continental Shelf offshore Massachusetts, USA, *Mar. Geol.*, *303–306*, 63–74.

Siegel, J., D. Lizarralde, B. Dugan, and M. Person (2014), Glacially generated overpressure on the New England continental shelf: Integration of full-waveform inversion and overpressure modeling, *J. Geophys. Res. Solid Earth*, *119*, 3393–3409, doi:10.1002/2013JB010278.

Slomp, C. P, and P. V. Cappellen (2004), Nutrient inputs to the coastal ocean through submarine groundwater discharge: Controls and potential impact, *J. Hydrol.*, *295*, 64–86.

Spinelli, G. A., P. S. Mozley, H. J. Tobin, M. B. Underwood, N. W. Hoffman, and G. M. Bellew (2007), Diagenesis, sediment strength, and pore collapse in sediment approaching the Nankai Trough subduction zone, *GSA Bull.*, *119*(3/4), 377–390, doi:10.1130/B25920.1.

Steckler, M. S., G. S. Mountain, K. G. Miller, and N. Christie-Blick (1999), Reconstruction of Tertiary progradation and clinoform development on the New Jersey passive margin by 2-D backstripping, *Mar. Geol.*, *154*, 399–420.

Uchupi, E., N. Driscoll, R. D. Ballard, and S. T. Bolmer (2001), Drainage of late Wisconsin glacial lakes and the morphology and late quaternary stratigraphy of the New Jersey-southern New England continental shelf and slope, *Mar. Geol.*, *172*, 117–145.

Vaikmae, R., L. Vallner, H. H. Loosi, P. C. Blaser, and M. Julillard-Tardent (2001), Paleogroundwater of glacial origin in the Cambrian-Vendian aquifer of northern Estonia, in *Paleowaters of Coastal Europe: Evolution of Groundwater since the Late Pleistocene, Spec. Publ.*, vol. 189, edited by W. M. Edmunds and C. J. Milne, pp. 17–27, Geol. Soc., London, U. K.

van der Veen, C. J. (1998), *Fundamentals of Glacier Dynamics*, A. A. Balkema, Rotterdam, Netherlands.

van Geldern, R., T. Hayashi, M. E. Böttcher, M. J. Mottl, J. A. C. Barth, S. Stadler (2013), Stable isotope geochemistry of pore waters and marine sediments from the New Jersey shelf: Methane formation and fluid origin, *Geosphere*, *9*, 96–112, doi:10.1130/GES00859.1.

Vidstrand, P., S. Follin, J. Selroos, J. Näslund, and I. Rhén (2013), Modeling of groundwater flow at depth in crystalline rock beneath a moving ice-sheet margin, exemplified by the Fennoscandian Shield, Sweden, *Hydrogeol. J.*, *21*, 239–255.

Williams, D. G., R. C. Thunell, E. Tappa, D. Rio, and I. Raffi (1988), Chronology of the Pleistocene oxygen isotope record: 0–1.88 m.y. B.P., *Palaeogeogr. Palaeoclimatol. Palaeoecol.*, *64*, 221–240.

Wilson, A., and C. Ruppel (2007), Salt tectonics and shallow subseafloor fluid convection: Models of coupled fluid-heat-salt transport, *Geofluids*, *7*, 377–386.

Yardley, G. S., and R. E. Swarbrick (2000), Lateral transfer: A source of additional overpressure?, *Mar. Pet. Geol.*, *17*, 523–537, doi:10.1016/S0264-8172(00)00007-6.